ORIGINAL PAPER

Mixed mode stable tearing of thin sheet Al 6061-T6 specimens: experimental measurements and finite element simulations using a modified Mohr-Coulomb fracture criterion

**Yaning Li · Tomasz Wierzbicki ·
Michael A. Sutton · Junhui Yan ·
Xiaomin Deng**

Abstract　In this investigation, a combined experimental and computational approach with a Modified Mohr Coulomb (MMC) fracture criterion employing post-initiation element softening is used to simulate stable crack propagation under Mode I, Mode III and combined Mode I/III loading conditions. Results from the studies demonstrate that good correlation exists between the measured load-displacement and the numerically predicted response when the stiffness of the specimen fixture is included in the FE model. The numerical results were able to capture most of the experimentally observed features during crack propagation, such as through-thickness slant fracture, necking, tunneling and local specimen twist, thus confirming that the MMC criterion is suitable for predicting in-plane and out-of-plane tearing of sheets. It was found that in order to predict correctly the load-displacement curve as well as the fracture plane, different amount of softening is needed for Mode I and Mode III loading cases. This observation can be justified on the micro-mechanical level, while there is a competition between the mechanisms of dimple and shear fracture.

Y. Li (✉) · T. Wierzbicki
Impact and Crashworthiness Lab, Department of
Mechanical Engineering, Massachusetts Institute of
Technology, Cambridge, MA 02139, USA
e-mail: yaningli@mit.edu

M. A. Sutton · J. Yan · X. Deng
Department of Mechanical Engineering, University
of South Carolina, Columbia, SC 29208, USA

1 Introduction

The problem of ductile crack initiation and propagation for a pre-cracked specimen, such as Compact Tension (CT) specimens, subjected to a single mode of loading (e.g., Mode I) has received a great deal of attention in the literature. Several methods, such as, cohesive elements, CTOD, CTOA, and the J-integral can predict fracture response with varying degrees of accuracy. Even though this area of fracture mechanics is well established, there is much less information in the literature regarding combined Mode I/II or Mode I/III response.

Parallel advances were made in the experimental part of this research. Two types of clamping fixtures developed for Mode I/II loading and Mode I/III loading, suitable for standard tensile rigs are shown in Fig. 1.

Presently, the displacement and the strain fields are measured by digital correlation system. Tearing tests on pre-crack specimens of the type shown in Fig. 1 provide a wealth of information needed to develop a suitable fracture model. Another type of equipment suitable for studying the mixed Mode I/II fracture is the modified Arcan fixture (Amstutz et al. 1995, 1997). In all of these studies, tests were performed on compact tension specimens so that crack initiation was not part of either the

Report Documentation Page

1. REPORT DATE **DEC 2009**	2. REPORT TYPE	3. DATES COVERED **00-00-2009 to 00-00-2009**

4. TITLE AND SUBTITLE **Mixed mode stable tearing of thin sheet Al 6061-T6 specimens: experimental measurements and finite element simulations using a modified Mohr-Coulomb fracture criterion**	5a. CONTRACT NUMBER
	5b. GRANT NUMBER
	5c. PROGRAM ELEMENT NUMBER
6. AUTHOR(S)	5d. PROJECT NUMBER
	5e. TASK NUMBER
	5f. WORK UNIT NUMBER
7. PERFORMING ORGANIZATION NAME(S) AND ADDRESS(ES) **Massachusetts Institute of Technology,Impact and Crashworthiness Lab,Department of Mechanical Engineering,Cambridge,MA,02139**	8. PERFORMING ORGANIZATION REPORT NUMBER
9. SPONSORING/MONITORING AGENCY NAME(S) AND ADDRESS(ES)	10. SPONSOR/MONITOR'S ACRONYM(S)
	11. SPONSOR/MONITOR'S REPORT NUMBER(S)

12. DISTRIBUTION/AVAILABILITY STATEMENT
Approved for public release; distribution unlimited

13. SUPPLEMENTARY NOTES

14. ABSTRACT
In this investigation, a combined experimental and computational approach with a Modified Mohr Coulomb (MMC) fracture criterion employing post-initiation element softening is used to simulate stable crack propagation under Mode I, Mode III and combined Mode I/III loading conditions. Results from the studies demonstrate that good correlation exists between the measured load-displacement and the numerically predicted response when the stiffness of the specimen fixture is included in the FE model. The numerical results were able to capture most of the experimentally observed features during crack propagation, such as through-thickness slant fracture, necking, tunneling and local specimen twist thus confirming that the MMC criterion is suitable for predicting in-plane and out-of-plane tearing of sheets. It was found that in order to predict correctly the load-displacement curve as well as the fracture plane different amount of softening is needed forMode I and Mode III loading cases. This observation can be justified on the micro-mechanical level, while there is a competition between the mechanisms of dimple and shear fracture.

15. SUBJECT TERMS

16. SECURITY CLASSIFICATION OF:			17. LIMITATION OF ABSTRACT	18. NUMBER OF PAGES	19a. NAME OF RESPONSIBLE PERSON
a. REPORT **unclassified**	b. ABSTRACT **unclassified**	c. THIS PAGE **unclassified**	**Same as Report (SAR)**	**19**	

Fig. 1 Special fixtures for combine Mode I/II (*left*, Aoki et al. 1990) and Mode I/III (*right*, Yan et al. 2009a) loading
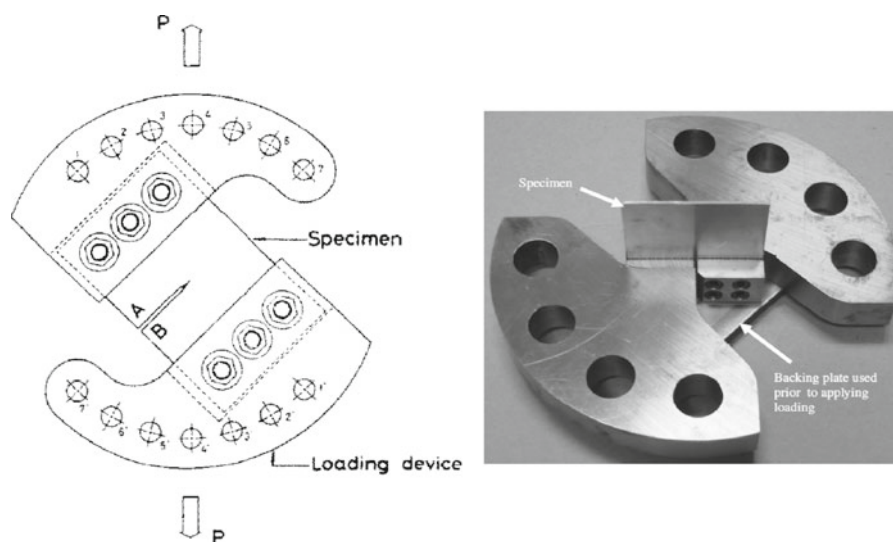
experiments or the predictions. Based on the experimental measurements, which included both the mixed mode crack opening displacement vector, COD, and the surface strain fields, a mode transition from tension-dominated to shear-dominated was identified. Based on these observations, a mixed mode COD criterion was proposed to predict both the initial crack growth and direction of crack extension (Ma et al. 1999; Sutton et al. 2000a,b). As part of these studies, the investigators noted that components of COD are most likely a function of constraint at the crack tip, resulting in a series of articles that focused on the underlying physics related to the combined effect of constraint and effective stress (Sutton et al. 2002; Zuo et al. 2004, 2005). This work was later extended into experimental, theoretical and numerical studies to describe the effect of tension-torsion loading on fracture of thin sheet materials (Sutton et al. 2001, 2007; Lan et al. 2007; Yan et al. 2007, 2009a,b) with additional focus on slant fracture and whether its presence/absence can be predicted using macroscopic quantities such as effective plastic strain or effective stress (Mahgoub et al. 2003; Lan et al. 2006).

In several recent publications, comparison was made between the numerical prediction and experimental results. Sutton et al. (2000a,b) employed their generalized CTOD method to predict crack growth during mixed Mode I/II fracture, with the direction of crack growth predicted using a specified ratio of COD components and the onset of crack growth defined by the magnitude of the critical COD.

The Cohesive Zone Model (CZM) provides also a practical way to predict mixed-mode fracture (Ortiz and Pandolfi 1999). De-Andre et al. (1999) demonstrated an application of cohesive elements to fatigue crack growth using a three-dimensional cohesive element with irreversible cohesive laws to track three-dimensional fatigue crack fronts. The simulation results were compared with the axial fatigue tests on aluminum shafts performed by Thompson and Sheppard (1992). Simonsen and Tornqvist (2004), reported on a combined experimental-numerical procedure to calibrate macroscopic crack propagation criteria (Rice and Tracey (1969) and a constant equivalent strain criterion) for large-scale structures, with an application to ship grounding. Oliver (1996a,b), Teng (2008) and Xue (2007a) reported on successful application of continuum damage mechanics in simulating initiation and propagation of cracks. An alternative approach is being developed by Belytschko and his followers using the concept of Extended Finite Element method (XFEM) (Moes and Belytschko 2002; Gravouil et al. 2002). Other less general numerical methods are also proposed, for example, (Morrissey and Geubelle 1997; Gao and Klein 1998; Oliver 1996a,b).

More recently, Bai and Wierzbicki (2010) extended the Mohr-Coulomb failure criterion (MMC) and introduced an explicit dependence of the equivalent strain to fracture on both the stress triaxiality and Lode angle parameter. The Lode angle θ is proportional to the normalized third invariant of stress deviator. This fracture criterion includes three parameters which are calibrated

from a limited number (minimum three) of experiments. The MMC method is an alternative to the widely used GTN model, which requires different types of parameters to be determined from experiments.

Several people in the ICL lab contributed to the development of the MMC fracture model, which is the current working model in the lab. Bao and Wierzbicki (2004) constructed an empirical fracture diagram in a wide range of stress triaxiality based on the results of 36 meticulous experiments and numerical simulations of several types of specimens. More recently, Xue (2007b) and Xue and Wierzbicki (2008) introduced the dependence of the fracture strain on the Lode angle and constructed a general form of an asymmetric fracture model. Bai and Wierzbicki (2010) showed that the three dimensional fracture locus could be derived in a simple and elegant way from the modified Mohr-Coulomb failure criterion. The post-failure model was developed and applied to the plane strain initiation and propagation of cracks by and Li and Wierzbicki (2010a). Finally, MMC model was calibrated for several grades of Advanced High Strength Steels (AHSS). The validation of this model in sheet metal forming operations was presented in three recent publications (Li et al. 2010b; Luo and Wierzbicki 2010). For the sake of economy space, the details of the derivation of MMC are not given in this paper. The interested reader is referred to the above original publications.

It is noted that all plasticity and fracture parameters used in the numerical simulations were obtained from an entirely independent set of experiments performed at MIT (Beese et al. 2010), whereas the experiments being simulated were performed at USC and NASA. Thus, the comparison of the predicted and measured load-displacement curve is an essential part of the validation process for the simulations.

In this study, the MMC stress-strain based fracture criteria is used to simulate crack propagation under nominally Mode I, Mode III and combined Mode I/III conditions. An extensive comparison is made with experiments performed by Yan et al. (2009a,b) using Al6061-T6 sheet specimens.

2 Material model

All specimens were manufactured using 6061-T6 aluminum alloy, which was extensively studied by the present authors at Massachusetts Institute of Technol-
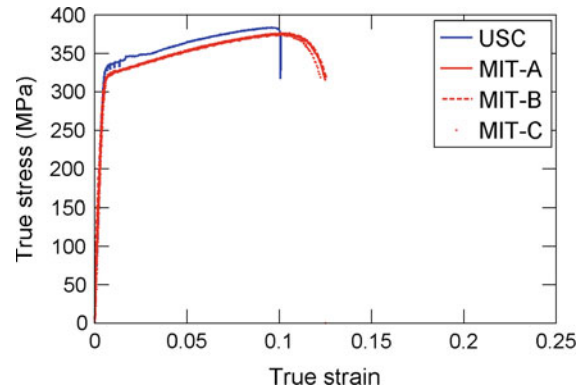
Fig. 2 Stress-strain data for Al6061-T6 (all simulations in this paper used the averaged MIT data)

ogy (MIT) and the University of South Carolina (USC). Though the material used at both laboratories came from different batches, the measured hardening curves (red at MIT, blue at USC) are quite similar, as shown in Fig. 2. Baseline experiments performed at MIT by extracting dog-bone specimens at 0°, 45° and 90° from the sheet rolling direction indicated the presence of weak anisotropy. In this study, all simulations were performed using a standard J2 plasticity model with the averaged MIT stress-strain curve and without considering anisotropy in the stress-strain response. The finite element calculations were performed by ABAQUS6.8/Explicit which is a nonlinear FE code for large plastic strain.

3 Fracture model

The fracture model used in these simulations was described in previous work (Bai and Wierzbicki 2010; Beese et al. 2010; Li and Wierzbicki 2010a; Li et al. 2010b; Li and Wierzbicki 2009). According to this model, fracture in a given element is assumed to occur when the accumulated normalized plastic strain reaches unity

$$D = \int_{0}^{\overline{\varepsilon}_f} \frac{d\overline{\varepsilon}_p}{f(\eta, \overline{\theta})} \tag{1a}$$

where $\overline{\varepsilon}_p$ is the equivalent plastic strain, $\eta = \frac{\sigma_m}{\overline{\sigma}}$ stands for stress triaxiality, σ_m is the mean stress, $\overline{\sigma}$ is the equivalent stress, and $\overline{\theta}$ is the Lode angle parameter,

which is defined as

$$\overline{\theta} = 1 - \frac{2}{\pi} \arccos\left(\left(\frac{r}{\sigma}\right)^3\right) \qquad (1b)$$

where r is the third invariant of the deviatoric stress tensor. The meaning of the denominator of the integrand of Eq. 1 becomes clear when we consider a class of proportional loading paths for which the parameters η and $\overline{\theta}$ are constant. In this case, Eq. 1 is reduced to $\overline{\varepsilon}_f = f(\eta, \overline{\theta})$ after integration. Thus the normalizing function in the denominator of Eq. 1 represents the magnitude of the equivalent fracture strain which is reached by all possible proportional loading paths.

The general expression for the equivalent strain to fracture as a function of the stress triaxiality and Lode angle parameters, derived from the MMC model is

$$\overline{\varepsilon}_f(\eta, \overline{\theta}) = \left\{\frac{A}{C_2}\left[C_3 + \frac{\sqrt{3}}{2 - \sqrt{3}}(1 - C_3)\right.\right.$$
$$\times \left(\sec\left(\frac{\overline{\theta}\pi}{6}\right) - 1\right)\left]\left[\sqrt{\frac{1 + C_1^2}{3}}\right.\right.$$
$$\times \cos\left(\frac{\overline{\theta}\pi}{6}\right) + C_1\left(\eta + \frac{1}{3}\sin\left(\frac{\overline{\theta}\pi}{6}\right)\right)\right]\right\}^{\frac{1}{n}}$$
$$\qquad (2)$$

There are three fracture constants in the above equation, C_1 C_2 and C_3 that could be determined from a minimum of three tests. In the present problem, five different tests were performed which increases the accuracy of the fracture locus.

Since the specimen used in the Mode I/III experiments is relatively thin, plane stress is a reasonable assumption. In this case, the MMC fracture model yields the following set of equations (see Bai and Wierzbicki 2010).

$$\overline{\varepsilon}_f(\eta) = \left\{\frac{A}{C_2}f_3\left[\sqrt{\frac{1 + C_1^2}{3}} \cdot f_1\right.\right.$$
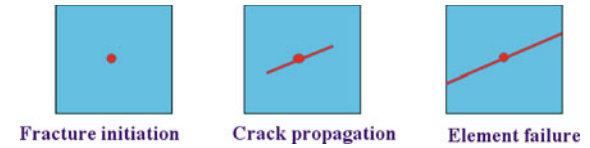$$\left.\left. + C_1\left(\eta + \frac{f_2}{3}\right)\right]\right\}^{-\frac{1}{n}} \qquad (3)$$

$$f_1 = \cos\left\{\frac{1}{3}\arcsin\left[-\frac{27}{2}\eta\left(\eta^2 - \frac{1}{3}\right)\right]\right\} \qquad (3a)$$

$$f_2 = \sin\left\{\frac{1}{3}\arcsin\left[-\frac{27}{2}\eta\left(\eta^2 - \frac{1}{3}\right)\right]\right\} \qquad (3b)$$

$$f_3 = C_3 + \frac{\sqrt{3}}{2 - \sqrt{3}}(1 - C_3)\left(\frac{1}{f_1} - 1\right). \qquad (3c)$$

Table 1 Calibrated material and fracture parameters for Al6061-T6

A	n	C_1	C_2	C_3
438 MPa	0.07	0.06	228 MPa	0.93

Fig. 3 The concept of the simulation of post-initiation behavior of an element (Li and Wierzbicki 2010a)

In the above equations, n is the hardening exponent obtained using the uniaxial data in Fig. 2, The amplitude of the hardening law is denoted by A and the three model parameters C_1, C_2, C_3 related to the functional form of the critical fracture strain are to be determined from a series of fracture experiments. A set of plasticity and fracture parameters, determined by Beese et al. (2010) for Al6061-T6 and used in the present simulations, are shown in Table 1.

The graphic representation of Eq. 3 is shown in Fig. 19. There are four segments of the fracture locus, each represented by a different color in Fig. 19.

4 Post-initiation behavior of an element

In order to describe the formation of slant fracture, some type of post-initiation softening must be assumed (Li and Wierzbicki 2010a). One can define two types of softening, one originating from material weakening due to void growth and linkage. This type of softening has been extensively studied in the literature. In addition to the existence of softening process at the material level, one can interpret the softening at the level of a finite element. This is illustrated in Fig. 3.

Fracture is assumed to initiate at one point within an element. Because of a finite size of the element, additional work is needed to propagate the crack through the element. The local material (finite element) gradually loses strength as crack propagates through the element and reaches the element boundary when total separation finally occurs. The above interpretation of "structural" softening has led to a realistic model of the fracture process that allowed

the investigators to successfully predict the onset of slant fracture (Li and Wierzbicki 2010a). In the present paper, the post-initiation model available in ABAQUS V6.8 will be used. This model involves only one scalar parameter u_f that may change from one loading case to the other. For example, we have found that larger values of u_f should be used for Mode I and smaller values for Mode III fracture, with instantaneous fracture corresponding to $u_f = 0$. The larger the parameter u_f, the longer post-initiation lasts. In our present numerical simulations, different values of u_f were used, ranging from $1e^{-5}$ to 0.1 (see Sect. 10.2).

5 Description of experiments

All mixed mode I/III experiments were performed in an MTS 810 load frame under displacement control, see Fig. 4. The experimental set-up consists of securely attaching the specimen to two quarter circle fixtures. The fixtures are connected to the loading frame through pins that are inserted in loading clevises, see Fig. 5. The clevises in turn are clamped into the hydraulic grips of the loading frame. Depending on the position of the pin with respect to the fixtures, one can generate Mode I, Mode III and combined Mode I/III far field loading conditions. The position of the pins is characterized by the loading angle Φ, defined in Fig. 4. The value $\Phi = 0\circ$ corresponds to Mode I loading, while $\Phi = 90°$ provides nominally far-field Mode III conditions. The intermediate angles $\Phi = 30°$ and $\Phi = 60°$ generate combined Mode I/III fracture.

In this work, three-dimensional Digital Image Correlation (3D-DIC) is used to obtain surface displacement measurements in the crack tip region in these experiments. The 3D-DIC system is shown in Fig. 4. Before performing each experiment, a high contrast random pattern of speckles is applied to each specimen and the 3D-DIC system is positioned to view the crack tip region. Prior to performing each experiment, both cameras are synchronized and calibrated. A photograph of the as-painted undeformed specimen, as well as a photograph of a deformed and fracturing specimen with $\Phi = 60°$, are shown in Fig. 6.
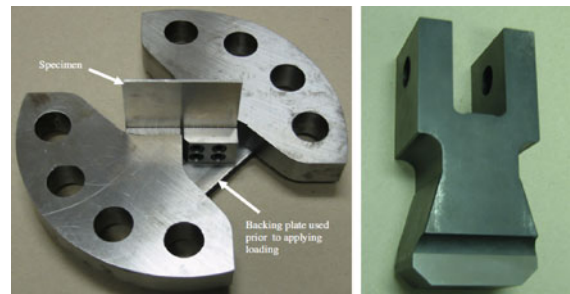
6 FE modeling

Two models were developed by discretizing the deformable part of the specimen, using either solid

1—Camera 0, 2—Camera 1, 3—Translation Stage, 4—Hydraulic Grip 5—Clevis, 6—Fixture, 7—Specimen, 8—Light Source, 9—Rotation Constraint, 10—extension bar

Fig. 4 Experimental setup for combined tension-torsion loading of thin specimen

Fig. 5 Photos of specimen fixture (*left*) and the clevis connecting the fixture with the cross-head of the testing machine (*right*)

or shell elements. Both models have a refined central part along the expected path of the crack. Outside this region, a much coarser mesh was used. The solid element is eight nodes with reduced integration (C3D8R in ABAQUS). The shell element is four nodes with reduce integration (S4R in ABAQUS). In the base FE model, the solid element size was very small, equal to 0.0625 mm in the critical region along the crack path. Other models with larger mesh size will be discussed in the following sections. In all cases there were 5 elements through the thickness. Altogether there were about 38,000 elements in the base model. A representative undeformed mesh is shown in Fig. 7. It is remarked that the choice of the number of

Fig. 6 Dimensions of the undeformed specimen (*left*) and the deformed specimen with about 20 mm crack extension during a mixed mode I/III experiment at loading angle $\Phi = 60°$
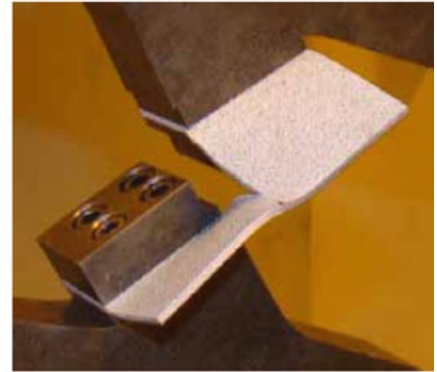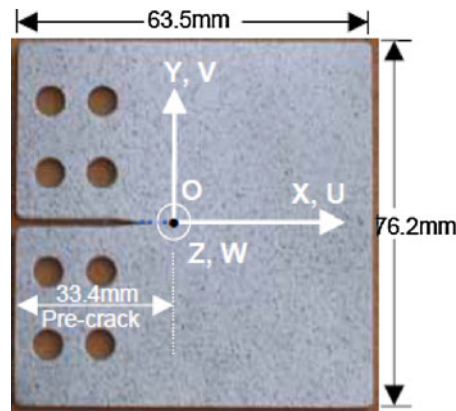
elements through the thickness was made as a compromise between accuracy and CPU time. Five elements through the thickness are sufficient to simulate slant fracture, which was one of the purposes of this paper.

For modeling purposes, the parts of the specimen bolted to the lower and upper fixtures were assumed to be "rigid" and represented by two reference points (see blue dots in Fig. 7). The two reference points are tied to the interface of the rigid part and the deformable part of the specimen. Since the lower fixture is much stiffer than the specimen, the investigators opted to use a '*U-joint connector*' option available in ABAQUS to conveniently represent the behavior of the connection to the clevises, see Fig. 8. It should be noted that a major advantage of using the *connector* concept to describe the overall behavior of the lower fixture is that ABAQUS allows the investigator to incorporate "stiffness variables" (e.g. rotational stiffnesses K_1 and K_2). These variables provide the opportunity to simplify the incorporation of complex joint/fixture behavior into the simulations. For example, the investigators observed effects such as slippage and small specimen rotation within the "rigid" bolted connection that would affect the overall response but are difficult to model accurately unless model parameters are used to represent these effects.

The control variables in the experiment and simulation are the vertical displacements of the pins. The output parameters of the finite element simulation are the relationship between the total reaction force and the pin displacement, the trajectory of the crack and a complete set of information about the stress, strain and displacement field around the crack tip. This allows for

a thorough comparison with experiments where many of the above parameters were measured.

7 Formulation of boundary conditions

As shown in Fig. 4, the thin specimen is firmly clamped to the fixture (component 6 in Fig. 4) with eight bolts, the clevis (component 5) is attached to the hydraulic grip (component 4) via high pressure clamping plates and the upper fixtures (component 6) is attached to the upper clevis through an "extension bar" (component 10). Both experimental observations and inspection of the design drawings suggest that there is a fair amount of flexibility in the overall experimental configuration (e.g., pin connections between the clevis-extension bar-upper lower fixture; slight specimen rotation due to slippage within lower fixture). This suggests that, while the displacements are continuous at all junctures, finite rotational flexibility must be considered to account for this effect when modeling the overall configuration. In fact, our simulations clearly show that the load-displacement curves and displacement-crack propagation results are highly sensitive to the rotational boundary conditions, requiring inclusion of the deformable connections into the computational model.

Figure 8 shows the FE model for the combined loading cases with loading angle Φ. Rotational flexibility of the clevis is modeled via the U-joint connectors between the pins and the reference points of the rigid part of the specimen, using the stiffness values defined in the Appendix and constraining the translational degrees of freedom.

**Fig. 7** Mixed mode I/III fracture specimen and our finite element model
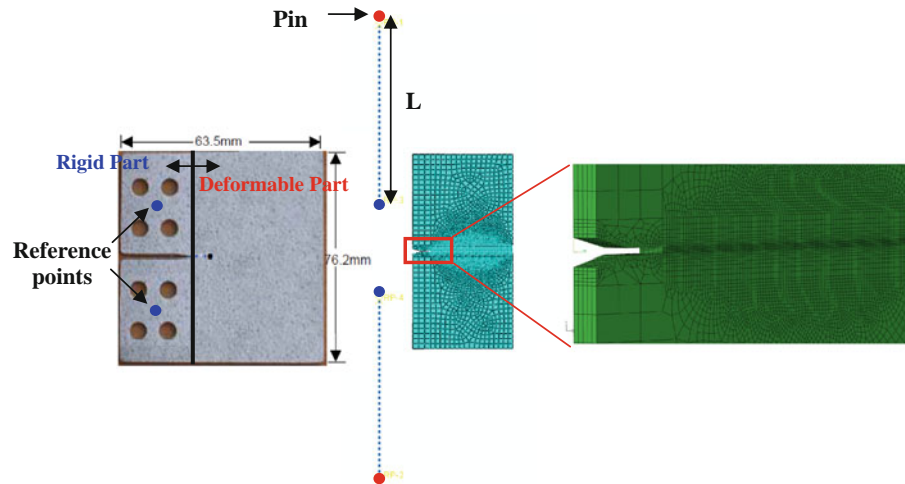
Fig. 8 Specimen and loading configuration for combined Mode I/III loading
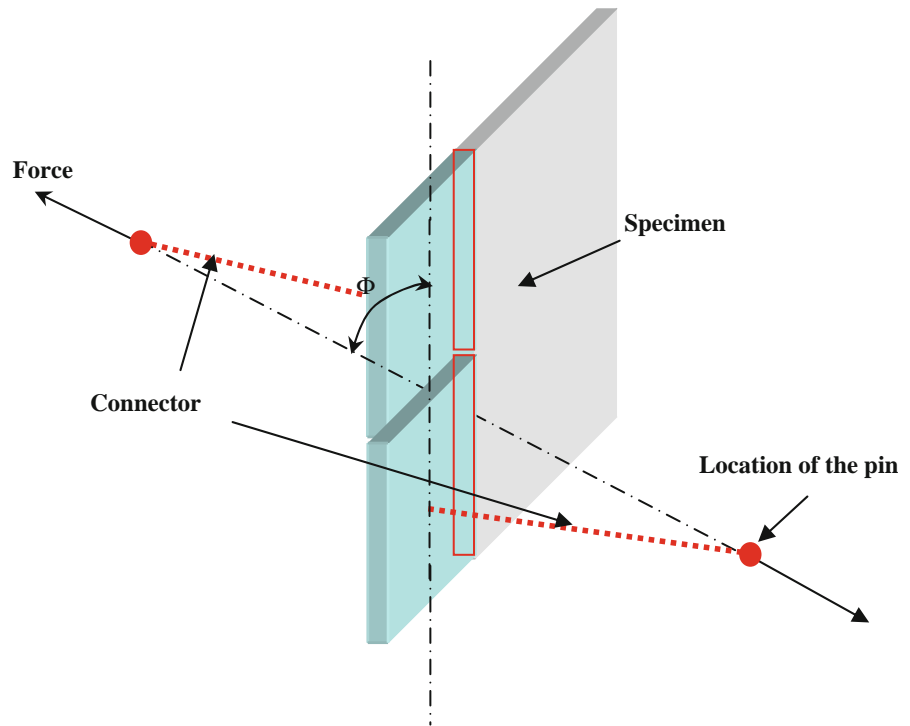
Using the *global (laboratory) coordinate system* shown on the clevis in Fig. 9, the bending moment vector, $\underline{M}$, has components in the *global (laboratory) system* (M_1, M_2, M_3). If all rotations are constrained, then all three components of the bending moment would be transmitted to the specimen. In addition to the global coordinate system, a *local (material) coordinate sys-* *tem* is defined which is attached to the specimen, as shown in Fig. 9. In this coordinate system, the bending moment vector is $\underline{M}'$ with components (M_1', M_2', M_3'). Assuming zero friction between the pin and the clevis, then $M_3 = M_3' \approx 0$ and the 3-D problem is reduced to the 2-D planar transformation of bending moments.
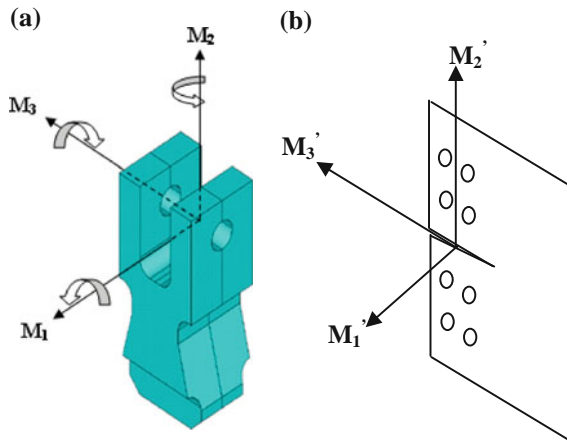
Fig. 9 Definition of global and local coordinate systems **a** Global (laboratory) coordinate system, **b** local (material) coordinate system

$$M'_1 = M_1 \cos \Phi + M_2 \sin \Phi$$
$$M'_2 = -M_1 \sin \Phi + M_2 \cos \Phi \qquad (4)$$

where the relative position of the two coordinate systems is uniquely defined by the angle Φ shown in Figs. 4 and 8.

The moment M'_1 represents an in-plane bending moment in the specimen whereas M'_2 represents the expected out-of-plane bending. It is noted that one physical source for the moment M_2 is the resistance of the arms of the fork to twist (Appendix). Of particular concern is the component M_1 which, when transferred to the specimen system, contributes to 'in-plane bending' of the specimen. The component M_1 could result from any combination of (a) incremental slippage within the bolted fixture-specimen connection causing in-plane rotation of the separate arms of the specimen, (b) non-zero clearance between lower fixture and clevis allowing rigid body rotation of fixture (see Fig. 9) and/or (c) finite flexural stiffness of each clevis fork arm.

It is assumed that the moment vector $\underline{M}'$ is related to the corresponding rotation $\underline{\theta}'$ through a linear transformation:

$$\underline{M} = \underline{K}\,\underline{\theta} \qquad (5a)$$
$$\underline{M}' = \underline{K}'\,\underline{\theta}', \qquad (5b)$$

where $\underline{K}$ and $\underline{K}'$ are stiffness matrices respectively in the global and material coordinate systems. Assuming uncoupled rotational stiffness factors, the stiffness matrices $\underline{K}$ and $\underline{K}'$ become diagonal:

$$\underline{K} = \begin{bmatrix} K_1 & 0 & 0 \\ 0 & K_2 & 0 \\ 0 & 0 & K_3 \end{bmatrix} \quad \underline{K}' = \begin{bmatrix} K'_1 & 0 & 0 \\ 0 & K'_2 & 0 \\ 0 & 0 & K'_3 \end{bmatrix} \qquad (6)$$

Letting $K'_3 = 0$ (free clevis pin rotation), the above system reduces to

$$M'_1 = K'_1 \theta'_1$$
$$M'_2 = K'_2 \theta'_2 \qquad (7)$$

In order to study how sensitive the load-displacement curves are to the stiffness matrix, limiting cases of the springs, pinned or fixed (zero stiffness or infinite stiffness) are investigated for both nominally Mode I and Mode III loading. The actual values of K'_1 and K'_2 are between the limiting cases and are estimated in the Appendix.

## 8 Finite element simulations

Since MMC is a strain based fracture criteria, the colors in all of the contours of the FE results shown in this paper represent the equivalent plastic strain, red is maximum and blue is minimum.

8.1 Effects of stiffness parameters

Four simulations of Mode I tensile tests were performed using different values for the constant K_1 using the eight-node solid element with reduce integration (C3D8R in ABAQUS) and the standard mesh with $\sim$ 38,000 elements. The corresponding load-displacement curves and the experimental data are shown in Fig. 10a. The line corresponding to the infinite stiffness (full rotational fixity) over-predicts the test results by a factor of two. At the same time, by releasing the rotational degree of freedom ($K_1 = 0$) the specimen resistance is underestimated. The simulations of the two extreme values of the planar rotational stiffness demonstrate that the clamping device of the specimen can not be assumed to be perfectly rigid. Additional simulations for two intermediate values of the rotational constant K_1 introduced a dramatic improvement in the accuracy of the numerical prediction.

It is noted that the Mode I response is practically a planar problem so that torsional stiffness of the clevis K_2 does not influence the solution. By contrast, the torsional stiffness has an effect on all

Fig. 10 The effects of finite stiffness **a** K_1 effect for tension loading; **b** K_2 effect for torsional loading; **c** K_2 effect for $\Phi = 30°$ loading; **d** K_2 effect for $\Phi = 60°$ loading
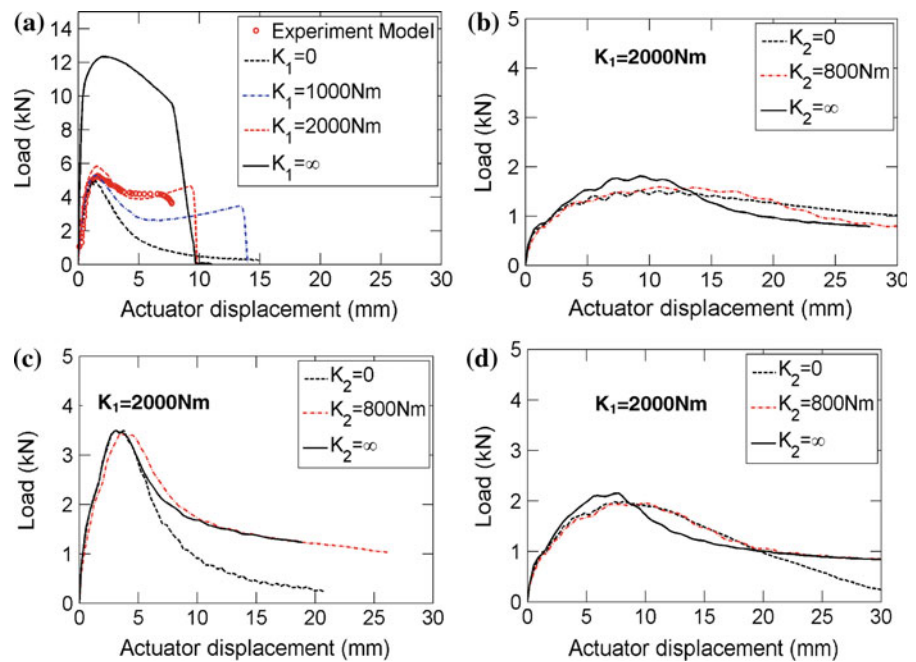
other loading cases (see Fig. 10b–d). For example, the response for shear loading was simulated using the estimated value of the bending stiffness for the fixture $K_1 = 2,000$ Nm (see the Appendix) and three different values of the torsional spring constants (see legend of Fig. 10b). Generally, the curve corresponding to the estimated value of the torsional stiffness $K_2 = 800$ Nm, lies between the two extreme cases of zero and infinite stiffness. Clearly the effect of torsional stiffness is pronounced but is not as strong as the effect of K_1 on Mode I response. Similar conclusions can be drawn for the combined loading cases shown in Fig. 10c and d. Based on the above parametric study, the values $K_1 = 2,000$, $K_2 = 800$ Nm and $K_3 = 0$ will be used for other loading cases (30 and 60 degree).

8.2 Comparison with experimental measurements

All simulations were performed with ABAQUS6.8 using the eight-node solid element C3D8R and a standard mesh (see Fig. 7).

8.2.1 Load-displacement

Comparison between the measured and calculated load-displacement curve for all four cases is shown in Fig. 11, taking the optimum values of the stiffness matrix obtained from the above parametric study. The correlation is good for all loading angles, providing confidence that the simulations are capable of adequately transferring global load conditions to the specimen for a wide range of loading angles, initiation of crack growth and a large range of crack extensions. The inserted color coded pictures in Fig. 11 show the deformed shape of the specimen in an intermediate stage of crack propagation for all four loading angles.

8.2.2 Crack path

Within the scope of the present element deletion technique, crack growth is considered as a sequence of crack initiation. In order to delete a given element, the accumulated damage should reach the critical value and the load carrying capacity must vanish in the post-initiate range. It should be noted that in the above

**Fig. 11** Results of numerical simulations for four values of the loading angle Φ
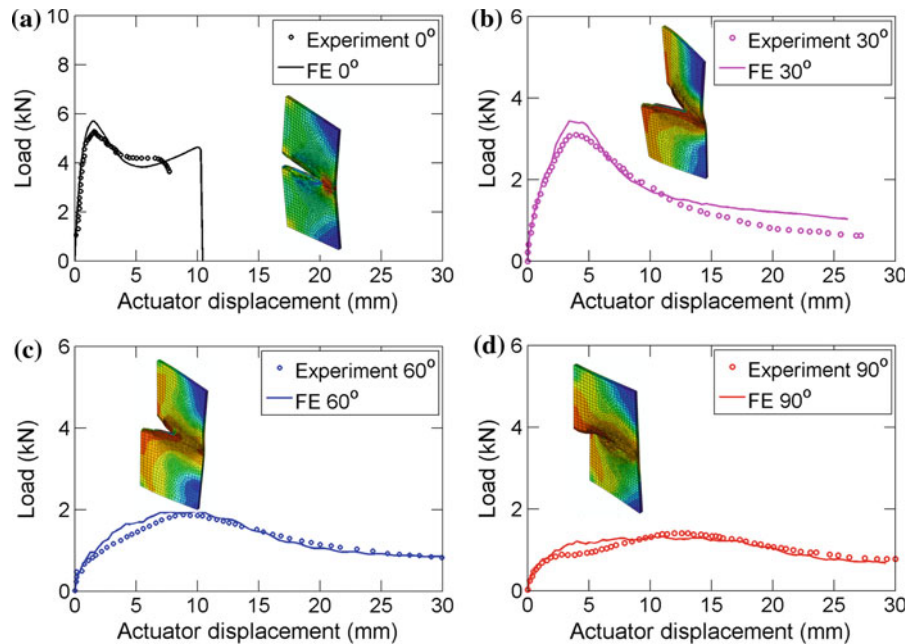
approach, the constraints at the crack tip (defined by stress triaxiality and Lode angle parameter may change in the course of the deformation of a given element. The predicted crack path is straight because of the assumed symmetry of the boundary conditions on both sides of the specimens and in generally good agreement with experimental evidence. It must be noted that for mode III loading case, Yan et al. (2009a) observed a slightly curvilinear crack growth for $\Phi = 90°$. In their experiment, an extension bar was added to the load train between the upper clevis and fixture to provide better visual access for the stereovision measurements. Such a modification of the gripping system introduced asymmetry to the specimen loading by lowering the bending stiffness and changing the torsional stiffness of the upper clevis. Since it is difficult to quantify the amount of asymmetry, the authors opted for maintaining symmetry in the simulations by assuming that the lower and upper portions of the load train have the same stiffness values for all loading angles.

## 9 Comparison between solid and shell element model predictions

For large structures, the solid element models used in the previous sections are computationally expensive.

To determine whether the tearing process can be modeled with reasonable accuracy by shell elements, the present specimen was modeled by four-node shell elements with reduced integration (S4R). Five integration points were taken through the wall thickness. All other input parameters (e.g., planar mesh size, post-initiation parameter u_f, and material data) were taken to be the same as used with the solid element model. The element deletion rule for shell element was implemented, such that an element is deleted when all the integration points lose their strength.

Figures 12 and 13 presents a comparison of the modeling results for Mode I and Mode III loading, respectively. As shown in Figs. 12 and 13, both solid and shell models adequately capture the load-displacement behavior *before* fracture initiation. However, the shell element model do not accurately model crack propagation for either Mode I or Mode III loading. For Mode I loading, the shell element model predicts that crack growth starts much earlier than the solid element model; the load reached only half of the experimentally measured peak load, and the process of Mode I crack propagation is unstable after growth initiates. For the Mode III loading case, the shell element model correctly predicted crack initiation and the corresponding peak force. However, large discrepancies appear later during the crack propagation phase, as evidenced in Fig. 13.
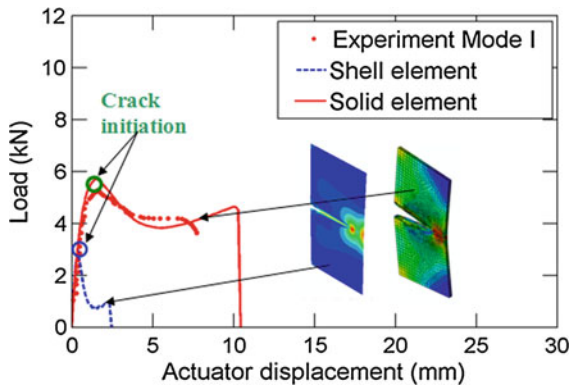
Fig. 12 Simulation results of shell element model and solid element model for Mode I loading
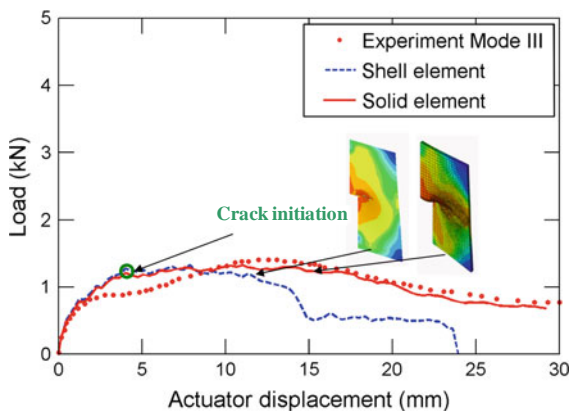
Fig. 13 Simulation results of shell element model and solid element model for Mode III loading

Based on our preliminary studies, it is clear that the shell element models are not suitable for predicting tearing process in sheets and hence all further model predictions will be based on the solid element model.

10 Parametric study

In this section, sensitivity analysis is performed on the effect of several modeling parameters on the finite element solution.

10.1 Influence of mesh size

Several solid model simulations were performed while maintaining a constant size of the solid element through the thickness and along the crack path equals 0.4 mm. At the same time, three mesh sizes were introduced

in the vertical direction equal respectively to 0.0625, 0.25 and 0.5 mm. For the case of Mode I fracture, there was little effect of mesh size on the load-displacement results. For Mode III response, there is a somewhat larger difference in specimen response between those three sizes of meshes, see Fig. 14.

In addition, there is a clear convergence of the results of the FE simulation for Mode I loading with diminishing mesh size. In the case of Mode III loading, the convergence is much slower. It can be concluded that the effect of mesh size of the global structure response with the present model is small. At the same time, the mesh size does influence the local response and in particular, the crack orientation. The experimentally observed slant fracture behavior cannot be predicted when the mesh size is too coarse. This is illustrated in Fig. 15, which compares results from two mesh sizes in the vertical direction, 0.25 and 0.0625 mm. In the case of 0.25 mm mesh, the fracture surface was flat and normal to the plane of the specimen, as shown in Fig. 15a. In order to generate slant fracture, a much smaller vertical mesh size (0.0625 mm) is necessary, as shown in Fig. 15b.

10.2 Influence of post-initiation parameter u_f

After crack growth occurs, elements near the initial growth site begin to gradually lose strength, resulting in "structural" softening. It was shown by Xue (2007a) and Li and Wierzbicki (2010a), that the presence of softening is necessary to simulate slant fracture. Two extreme values of the post-initiation parameter u_f were assumed to show the sensitivity of the solution; $u_f = 0.1$ mm and $u_f = 1e - 5$ mm. As shown in Fig. 16, changing u_f by four orders of magnitude produces only a moderate effect on the load displacement curve. It was found that a larger value is more appropriate for Mode I response, while a smaller value is needed for Mode III simulations. Indeed, the best fit of the experimental curve is obtained using $u_f = 0.1$ mm for Mode I, and $u_f = 0.01$ mm for Mode III.

The magnitude of u_f also affects the prediction of slant fracture during Mode I loading. Assuming $u_f = 1e - 5$ mm leads to a prediction of flat fracture even though the mesh size used is very fine (see Fig. 17a). At the same time, slant fracture is predicted when using a larger value $u_f = 0.1$ mm (Fig. 17b), which is physically more justified. It is thought that Mode I response
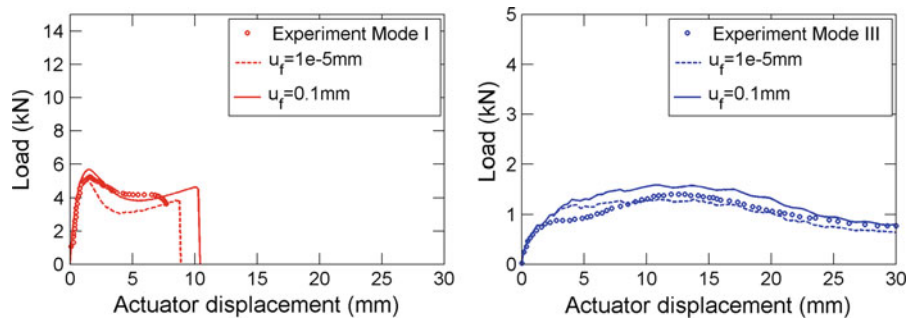
Fig. 14 Influence of mesh size on load-displacement curves. **a** Mode I, **b** Mode III
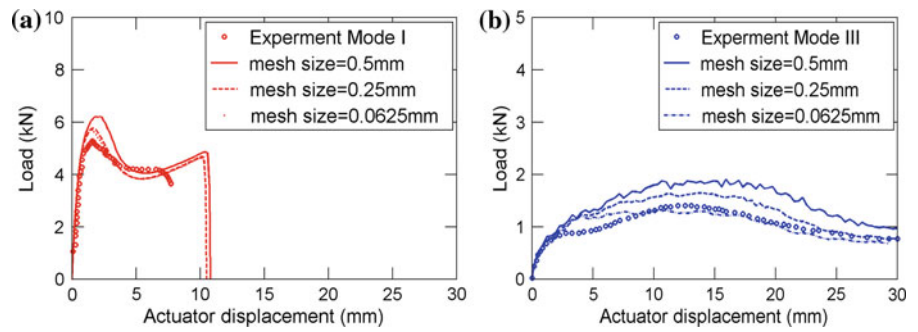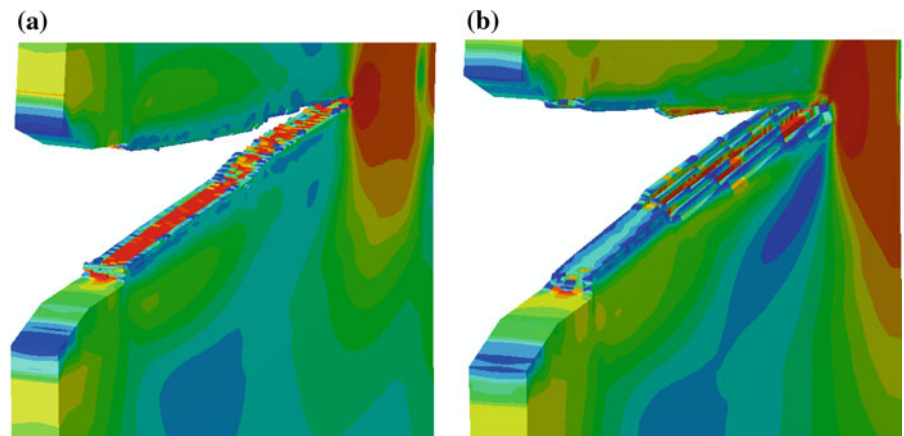

Fig. 15 Influence of mesh size on fracture surface for Mode I (both **a**, **b**) use $u_f = 0.1$). **a** Mesh size = 0.25 mmm, **b** Mesh size = 0.0625 mm
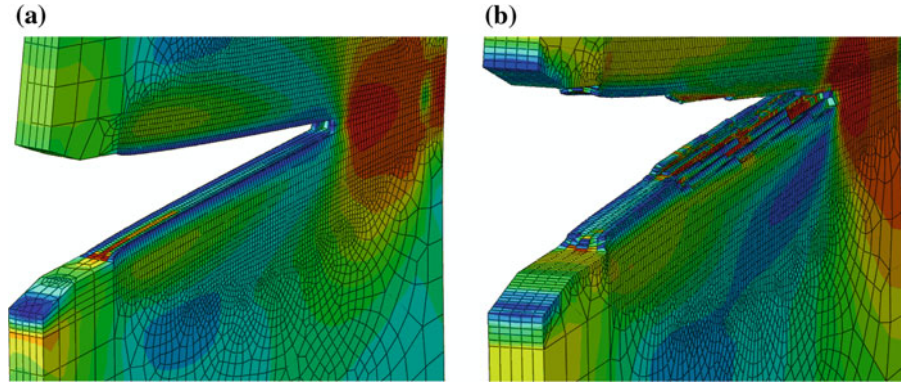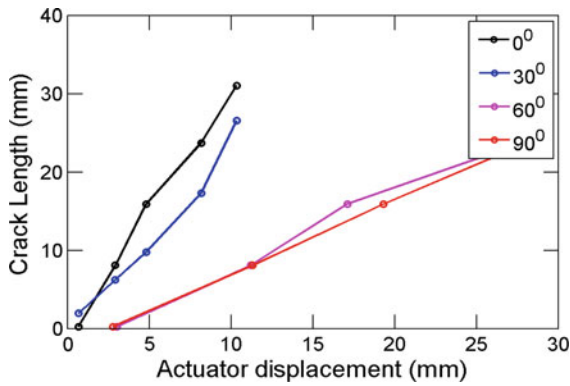

Fig. 16 Influence of u_f on load-displacement and fracture surface

Fig. 17 Influence of u_f on fracture surface for Mode I loading (both **a**, **b**) use fine mesh size, 0.00625 mm). **a** Flat fracture, $u_f = $ 1e-5 mm, **b** Slant fracture, $u_f = 0.1$ mm

Fig. 18 Crack extension vs. actuator displacement predicted by FE simulations

Fig. 19 Evolution of triaxiality and equivalent strain to fracture for Mode I and Mode III
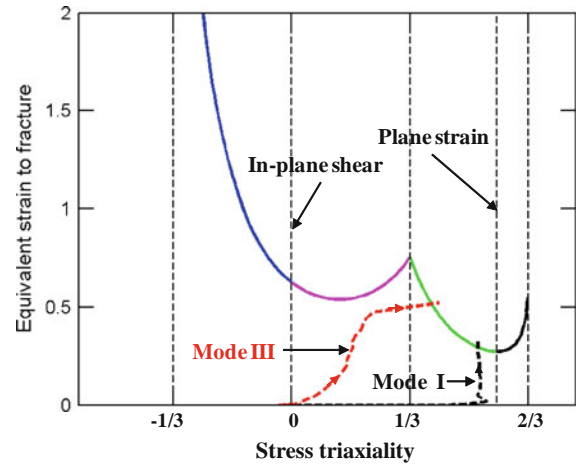
provide a better environment for the void growth and linkage which may take longer to lead to the final separation. As a result, the parameter u_f which controls the post-initiation range, should be larger. By contrast, Mode III loading promotes shear localization mechanism, which occurs more suddenly. Similar trend was observed by Li and Wierzbicki (2010a) when simulating plane strain fracture of TRIP steel.

Based on these studies, it appears that the magnitude of the softening parameter should be adjusted depending on the magnitude of stress triaxiality. In other words, the rate of element softening depends on the stress state at the crack tip. One can give here an analogy with the classical concept of Rice and Tracey (1969), where equivalent strain to fracture was found to be the diminishing function of stress triaxiality (high negative hydrostatic pressure)

11 Crack propagation

11.1 Crack length

One of the parameters that could be measured from the test is the amount of surface crack extension, see for example, Simonsen and Tornqvist (2004). Figure 18 presents the predicted crack length as a function of actuator displacement for all four loading angles. The predicted crack extension is almost linear. It is interesting to note that the actuator displacement-crack extension results for 60° and 90° almost coincide. Also, the trajectories for 0° and 30° are very similar. At the same time, the load-displacement responses for all four cases are quite distinct.
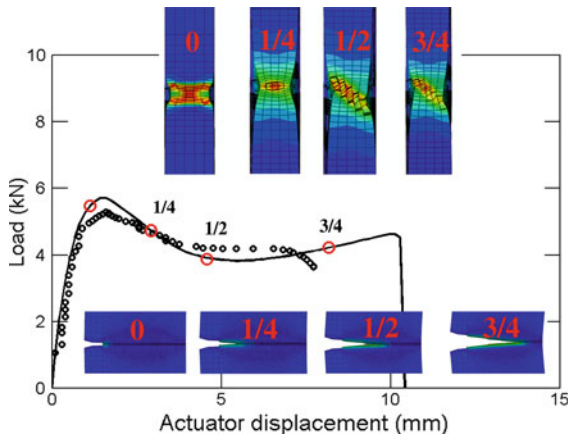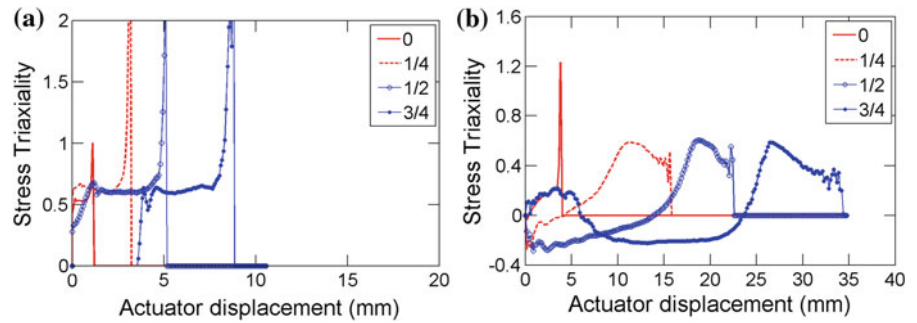
11.2 Evolution of stress triaxiality

According to the present fracture model, ductile fracture is a strong function of stress triaxiality η and Lode angle θ, which control the amount of stress constraint in the crack tip region. For the present plane-stress problem, the Lode angle is uniquely related to the stress triaxiality (see Bai and Wierzbicki 2010 and Li and Wierzbicki 2010a for details regarding this relationship), so it is sufficient to study the evolution of one parameter, which is taken to be η. The stress triaxiality, η, is a function of spatial position and loading history. The history of stress triaxiality for an element located at the intersection of the symmetry planes and the pre-crack tip is shown in Fig. 19. The trajectory lines approach the fracture locus defined by Eq. 3, and then cross it before fracture initiates. In Mode I loading, the stress triaxiality is approximately constant but never reaches the value 0.577 corresponding to plane strain (the pointed black dash line in Fig. 19). At the same time, for Mode III loading the parameter η starts from zero (as expected for pure shear loading) and then increases to a final value of 0.414 at the onset of fracture. This indicates that there is a gradual transition from pure shear at the beginning of the loading process to combine shear and tension later on. In other words, it is impossible to generate pure Mode III loading in the present type of tearing test, because there is a gradual transition from Mode III to combined Mode I/III loading.
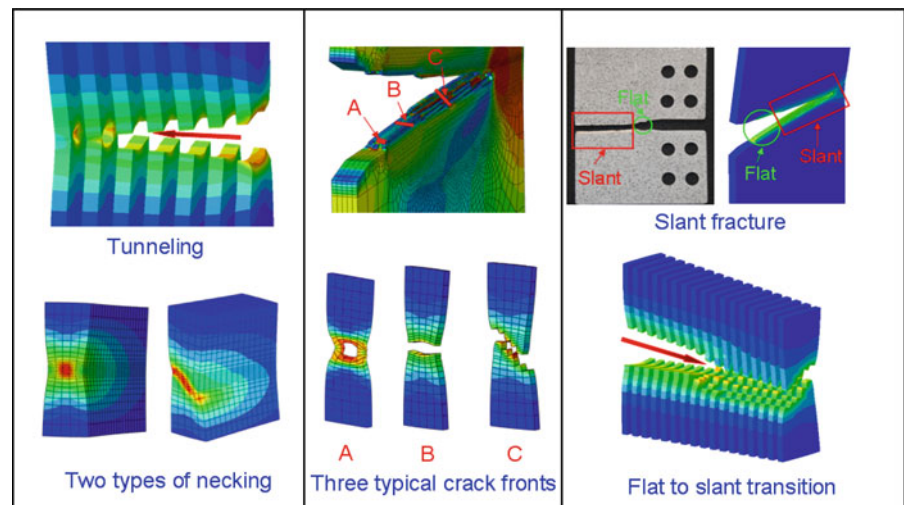
Fig. 20 Evolution of triaxiality for Mode I and Mode III at four different locations along the crack path. **a** Mode I, **b** Mode III

Fig. 21 Snapshots of cross sections at four locations showing necking, tunneling and shear band formation at the tip of the propagating crack for Mode I loading

The evolution of stress triaxiality for elements located along the crack path is shown in Fig. 20. Four elements are chosen for the analysis, located approxi-

mate at 0, 1/4, 1/2 and 3/4 width between the pre-crack tip and the end of the specimen. For Mode I, approximately all elements undergo similar histories of the parameter η. A sharp peak corresponds to the post-initiation behavior after which the equivalent stress $\bar{\sigma}$ diminishes from the maximum value to zero while the mean stress is approximately constant. Then, according to the definition of stress triaxiality, the parameter $\eta \rightarrow \infty$ and then the element is deleted immediately. A different situation is observed for Mode III. Elements close to the crack tip starts to deform under pure shear. Subsequently, twisting of the specimen takes place and the element located further away from the initial crack tip undergoes compression before returning back to tension, see Fig. 20b.

11.3 Detailed analysis of specimen deformation at the crack front

The results of the numerical simulation provide additional insight into the details of the predicted crack

Fig. 22 Details of the FE-captured behavior at the crack front for Mode I
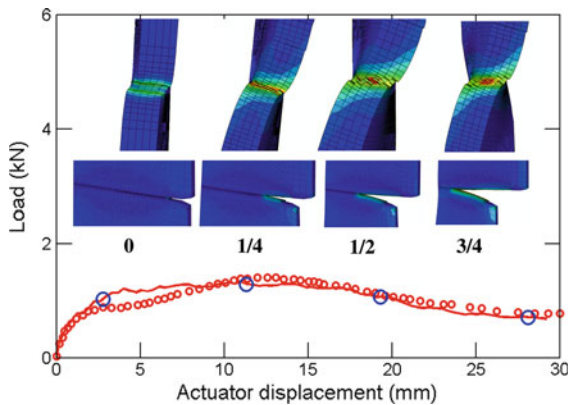
Fig. 23 Twists of the specimen in Mode III simulation

formation and propagation process. Snapshots of the deformed cross sections at four locations (the same locations as those shown in Fig. 20) along the width of the specimen for Mode I loading are shown in Fig. 21. From the deformed finite element mesh, one can clearly see a gradual transition from flat to slant fracture, formation of a shear band, local neck formation ahead of the crack, and crack tunneling. Those features can be detected when examining a partially fractured specimen.

A summary of various features of crack propagation captured by the FE simulations is given in Fig. 22, including necking, tunneling and flat to slant transition. Similar features were also predicted by Xue and Wierzbicki (2009) in the numerical simulation of CT specimen using fracture coupled with damage plasticity approach.

Different from Mode I, little thickness reduction is observed for Mode III loading, as shown in Fig. 23. The elements around the crack tip are deleted in the horizontal direction along the maximum shear starting from the free surface. At the same time, there is a gradual evolution of the twist of the specimen which causes a transition from a nearly pure Mode III into a combined Mode III/I. It can be concluded that the loading fixtures and thin sheet material will not readily generate pure Mode III conditions but rather a combination of two modes. This conclusion is consistent with a much earlier observation of Zhou and Wierzbicki (1996) that shear punching can be regarded as tensile deformation in the rotated coordinate system.

The final deformation predicted by FE simulation of the specimens under Mode III loads is compared with the photographs of the deformed specimen in Fig. 24, from different views. Because of the finite stiffness of the gripping system (K_2), the initially parallel edges of the specimen are subjected to twisting. The amount of calculated final twist compares very well with the actual specimen.

A comparison of the evolution of damage indicator through the thickness for both Mode I and Mode III before fracture at the cross-section in the middle of the specimen is shown in Fig. 25. For Mode I, damage initiates at the center and propagates outward through the thickness, whereas for Mode III, damage initiates from the surface and then propagates towards the center.

12 Discussion and conclusions

The quasi-static crack propagation in a modified CT specimen under combined Mode I and Mode III loads is studied both experimentally and computationally. The MMC fracture model is used to define a fracture initiation threshold for each element and element deletion is used in conjunction with a post-initiation softening model to predict crack growth along the experimentally observed crack path. It should be noted that the MMC model is not an ad hoc postulated model but a result of carefully planned and executed tests along with a suitable theoretical development. Furthermore, this model is now widely used in the automotive and steel industry for predicting initiation and propagation of cracks and sheets. The results of the present study indicate that by using the MMC fracture model with appropriate modifications of the gripping conditions, the load displacement response for all combined loading cases (0°, 30°, 60° and 90°) can be simulated with good accuracy. Also, all the local features of the specimen deformation around the crack tip such as thinning, tunneling and transition from flat to slant fracture were predicted with a great realism.

It was shown that slight variations in boundary conditions will have a major effect on the transfer of load from the grips to the crack tip region, and hence on the load-displacement response of the specimen. Specifically, it is found that the load-displacement response of Mode I is very sensitive to the planar rotational degrees of freedom whereas the Mode III loading configuration exhibits less sensitivity to boundary condition variations, though the effects need to be taken into consideration when modeling the entire specimen and grip

Fig. 24 Comparison of specimen deformation of FE simulations and Experiments of Mode III **a** simulation, **b** experiment
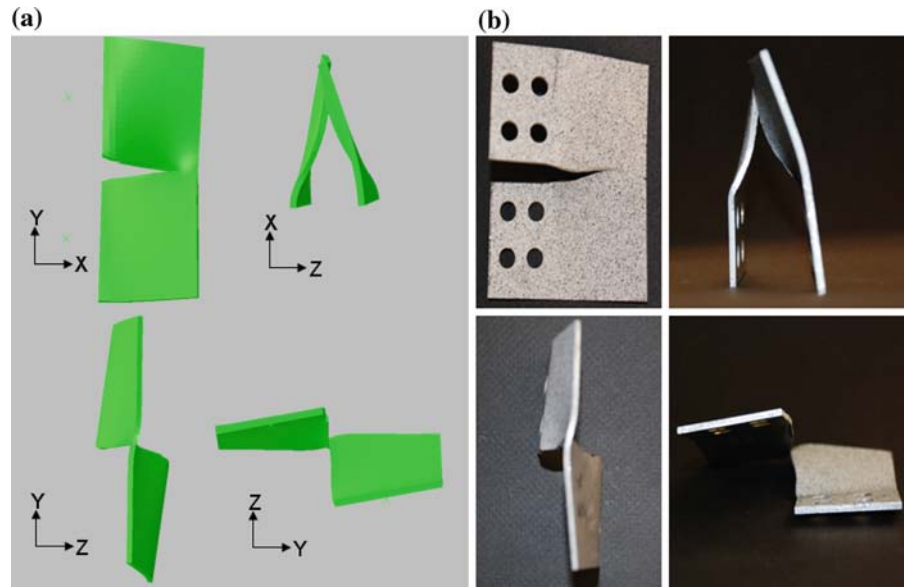
combination. Given the complexity of any joint configuration, the simulations suggest that a hybrid approach involving (a) a combination of experimental measurements (3D displacements on both sides) on the specimen in a region removed from the crack tip and (b) finite element analysis using smoothed displacement data input on a pre-defined boundary contour enclosing the crack tip and an assumed, through-thickness variation (e.g., linear variation) offers a way to mitigate the need to model the complex gripping conditions. At the same time, the boundary conditions provide sufficient input data to determine crack tip conditions with high fidelity. A similar approach was recently demonstrated by Yan et al. (2009a,b).

An extensive parametric study demonstrated that (a) solid elements must be used for fracture simulations in order to capture such effects as slant fracture, necking, tunneling, local twisting of the specimen under out-of-plane loading etc., (b) mesh size, element aspect ratio and post-initiation parameter u_f must be chosen carefully to predict formation of slant fracture. In particular, the magnitude of the post-initiation parameter u_f must be adjusted to account for the anticipated active ductile failure mechanism (void growth and linkage of voids or shear failure), suggesting that u_f is not a unique parameter but rather is a function of local conditions such as stress triaxiality.

Finally, our simulations demonstrate that it is not possible to generate a pure Mode III response using
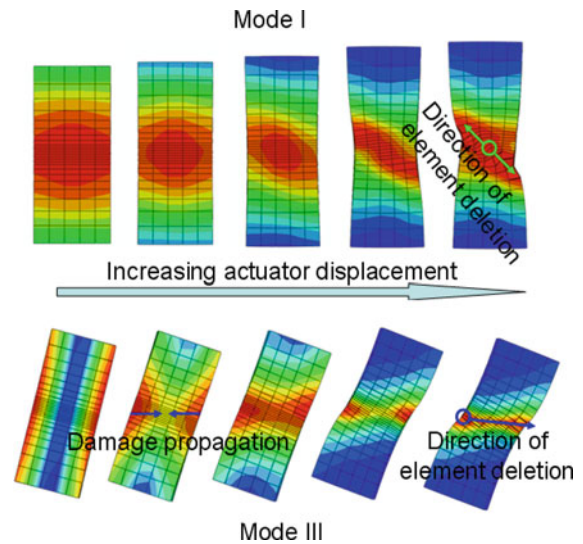
Fig. 25 Contour of the damage evolution through thickness for Mode I and Mode III

the present type of specimen and fixture. During the tearing process of thin sheets, the material is subject to torsional loading result in crack conditions that are a combination of modes, including both Mode I and Mode III.

A Appendix

A.1 Estimation of the stiffness K_1 with lower grip rotation in clevis

All elements connecting the specimen to the hydraulic grips are relatively solid and thus large bending rigidity. The rotational spring stiffness K_1 can be calculated by considering a simple model of a rigid fixture pressing onto one side of an elastic short cantilever beam, see Fig. 26.

During bending, the rigid fixture is exerting a force P at the tip of the clevis. A part of the loading is also transmitted by the pin. Consideration of the elastic deformation of the pin will lead to a statically indetermined problem which could be only solved numerically. In the simple derivation, it is assumed that the only contribution of the bending moment M at the root of the short cantilever comes from the contact force P:

$$M = Pl. \tag{A1}$$

From the simple beam theory, the rotation angle at the tip of the right arm of the fork is

$$\theta = \frac{Pl^2}{2EI}, \tag{A2}$$

where I is the moment of inertia of the rectangular cross section of the right arm of the fork with width b and thickness h (see Fig. 26).
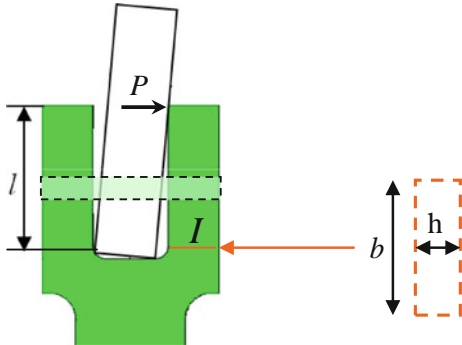
Fig. 26 Simple conceptual model of the stiffness of the fork joint

$$I = \frac{bh^3}{12}. \tag{A3}$$

Thus, the bending stiffness of the clevis can be written in the form;

$$K_1 = \frac{M}{\theta} \tag{A4}$$

Combining Eqs. (A1)–(A4), for the case without a pin,

$$K_1 = \frac{Ebh^3}{6l}. \tag{A5}$$

For the clevis used in the experiments, the dimensions are $l = b = 76.2$ mm and $h = 2.5$ mm. Since Young's modulus for the clevis material 17-4 stainless steel is $E = 210$ GPa, the bending component of the stiffness matrix of the clevis becomes $K_1 \approx 5.5 \times 10^2$ Nm.

It is clear that the pin contributes substantially to the stiffness of the entire joint. An order of magnitude analysis indicates that the above lower bound of the stiffness should be increased by the factor of 4. Therefore, in all subsequent calculations, the bending stiffness is assumed to be $K_1 \approx 2 \times 10^3$ Nm.

A.2 Estimation of the stiffness K_2

Since the pin makes the two arms of the fork twist together, then the polar moment of inertia for the rectangular section, with the length ratio b/h larger than 5 for each arm, is approximately

$$J = \frac{bh^3}{3}. \tag{A6}$$

The twist ratio (twist angle for uniform length)

$$\frac{d\phi}{dx} = \frac{M_t}{GJ} \tag{A7}$$

where M_t is the torque, and G is the shear modulus $G = \frac{E}{2(1+\nu)}$. Therefore, the torsional component of the stiffness of the fork (including both arms) is:

$$K_2 = 2\frac{GJ}{l} \approx \frac{Eh^3}{3(1+\nu)}. \tag{A8}$$

For the present geometry, the torsional stiffness becomes $K_2 \approx 800$ Nm. It should be noted that the torsional stiffness does not influence Mode I loading response, while for combined loading cases, the deformation of the specimen depends on both K_1 and K_2.

References

Amstutz BE, Sutton MA, Dawicke DS, Newman JC Jr (1995) An experimental study of CTOD for Mode I/Mode II stable crack growth in thin 2024-T3 aluminum specimens, fracture mechanics. American Society for Testing Materials (ASTM STP 1256) 26:256–271

Amstutz BE, Sutton MA, Dawicke DS, Boone ML (1997) Effects of mixed mode I/II loading and grain orientation on crack initiation and stable tearing in 2024-T3 aluminum, fatigue and fracture mechanics. American Society for testing Materials (ASTM STP 1296) 27:105–126

Aoki S, Kishimoto K, Yoshida M, Sakata M, Richard HA (1990) Elastic-plastic fracture behavior of an aluminum alloy under mixed mode loading. J Mech Phys Solids 38(2):195–213

Bai Y, Wierzbicki T (2010) Application of extended Mohr-Coulomb criterion to ductile fracture. Int J Fract 161:1–20

Bao Y, Wierzbicki T (2004) On fracture locus in the equivalent strain and stress triaxiality space. Int J Mech Sci 46:81–98

Beese AM, Luo M, Li Y, Bai Y, Wierzbicki T (2010) Partially coupled anisotropic fracture model for aluminum sheets. Eng Fract Mech 77:1128–1152

De-Andre A, Perez JL, Ortiz M (1999) Elastoplastic finite element analysis of three-dimensional fatigue crack growth in aluminum shafts subjected to axial loading. Int J Solids Struct 36:2231–2258

Gao H, Klein P (1998) Numerical simulation of crack growth in an isotropic solid with randomized internal cohesive bonds. J Mech Phys Solids 46(2):187–218

Gravouil A, Moes N, Belytschko T (2002) Non-planar 3D crack growth by the extended finite element and level sets-Part II: level set update. Int J Numer Methods Eng 53:2569–2586

Lan WM, Deng XM, Sutton MA, Cheng CS (2006) Study of slant fracture in ductile materials. Int J Fract 141:469–496

Lan WM, Deng XM, Sutton MA (2007) Three-dimensional finite element simulations of mixed-mode stable tearing crack growth experiments. Eng Fract Mech 74:2498–2517

Li Y, Wierzbicki T (2009) Mesh-size effect study of ductile fracture by non-local approach. In: Proceedings of the SEM annual conference. June 1–4, 2009 Albuquerque New Mexico, USA

Li Y, Wierzbicki T (2010a) Prediction of plane strain fracture of AHSS sheets with post-initiation softening. Int J Solids Struct 47(17):2316–2327

Li Y, Luo M, Gerlach G, Wierzbicki T (2010b) Prediction of shear-induced fracture in sheet metal forming. J Mater Process Technol 210:1858–1869

Luo M, Wierzbicki T (2010) Numerical failure analysis of a stretch-bending test on dual-phase steel sheets using a phenomenological fracture model. Int J Solid Struct 47(22–23):3084–3102

Ma F, Deng XM, Sutton MA, Newman JC Jr (1999) A CTOD-based mixed mode fracture criterion. ASTM STP 1359 on mixed mode crack behavior, pp 86–110

Ma F, Deng XM, Sutton MA, Fawaz SA (2001) Plane strain mixed mode crack-tip stress fields characterized by a triaxial stress parameter and a plastic deformation extent based characteristic length. J Mech Phys Solids 49:292–2953

Mahgoub E, Deng XM, Sutton MA (2003) Three-dimensional stress and deformation fields around flat and slant cracks under remote Mode I loading conditions. Eng Fract Mech 70:2527–2542

Moes N, Belytschko T (2002) Extended finite element method for cohesive crack growth. Eng Fract Mech 69:813–833

Morrissey JW, Geubelle PH (1997) A numerical scheme for Mode III dynamic fracture problems. Int J Numer Methods Eng 40:1181–1196

Oliver J (1996a) Modeling strong discontinuities in solid mechanics via strain softening constitutive equations part 1: 'Fudermentals'. Int J Numer Method Eng 39:3575–3600

Oliver J (1996b) Modeling strong discontinuities in solid mechanics via strain softening constitutive equations Part2: numerical simulation. Int J Numer Method Eng 39:3601–3623

Ortiz M, Pandolfi A (1999) Finite-deformation irreversible cohesive elements for three-dimensional crack-propagation analysis. Int J Numer Method Eng 44:1267–1282

Rice JR, Tracey DM (1969) On the ductile enlargement of voids in triaxial stress fields. J Mech Phys Solids 17:201–217

Simonsen BC, Tornqvist R (2004) Experimental and numerical modeling of ductile crack propagation in large-scale shell structures. Marine Struct 17:1–24

Sutton MA, Deng X Ma F, Newman JC Jr, James M (2000a) Development and application of a crack tip opening displacement-based mixed mode fracture criterion. Int J Solids Struct 37:3591–3618

Sutton MA, Boone ML, Ma F, Helm JD (2000b) A combined modeling-experimental study of the crack opening displacement criterion for characterization of stable crack growth under mixed mode I/II loading in thin sheet materials. Eng Fract Mech 66:171–185

Sutton MA, Helm JD, Boone ML (2001) Experimental study of crack growth in thin sheet material under tension-torsion loading. Int J Fract 109:285–301

Sutton MA, Ma F, Deng XM (2002) Mixed mode I/II crack-tip stress fields characterized by a triaxial stress parameter and a plastic deformation extent based characteristic length, fatigue and fracture mechanics: 33rd volume. ASTM STP 1417:233–268

Sutton MA, Yan JH, Deng XM, Cheng CS, Zavattieri P (2007) 3D Digital image correlation to quantify deformation and COD in ductile aluminum under mixed-mode I/III loading. Opt Eng 46(5):051003-1–051003-17

Teng X (2008) Numerical prediction of slant fracture with continuum damage mechanics. Eng Fract Mech 75(8):2020–2041

Thompson KD, Sheppard SD (1992) Fatigue crack-growth in notched and plain shafts subjected to torsion and axial loading. Eng Fract Mech 43:55–71

Xue L (2007a) Damage accumulation and fracture initiation in uncracked ductile solids subject to triaxial loading. Int J Solids Struct 44:5163–5181

Xue L (2007b) Ductile fracture modeling—theory, experimental investigation and numerical verification. PhD Thesis, Department of Mechanical Engineering, MIT

Xue L, Wierzbicki T (2008) Ductile fracture initiation and propagation modeling using damage plasticity theory. Eng Fract Mech 75(11):3276–3293

Xue L, Wierzbicki T (2009) Numerical simulation of fracture mode transition in ductile plates. Int J Solids Struct 46:1423–1435

Yan JH, Sutton MA, Deng XM, Cheng CS (2007) Mixed-mode fracture of ductile thin sheet materials under combined in-plane and out-of-plane loading. Int J Fract 144:297–321

Yan JH, Sutton MA, Deng X, Wei Z, Zavattieri P (2009a) Mixed-mode crack growth in ductile thin-sheet materials under combined in-plane and out-of-plane loading. Int J Fract 16:169–188

Yan JH, Sutton MA, Deng X, Zavattieri P, Wei Z (2009b) Mixed-mode crack growth in ductile thin sheet materials.

In: Proceedings of the SEM annual conference, June 1–4, 2009 Albuquerque New Mexico USA

Zhou Q, Wierzbicki T (1996) A tension zone model of blanking and tearing of ductile metal plates. Int J Mech Sci 38(3):303–324

Zuo JZ, Sutton MA, Deng XM (2004) Basic studies of ductile failure processes and implications for fracture prediction. Fatigue Fract Eng Mater Struct 27:231–243

Zuo JZ, Sutton MA, Deng XM (2005) Advances in tetrahedral mesh generation for modeling of three-dimensional regions with complex curvilinear crack shapes. Int J Number Methods Eng 63:256–275